Solar Wind Temperature Isotropy

P. H. Yoon,[1,2,3,*] J. Seough,[3] C. S. Salem,[4] and K. G. Klein[5]

[1]*University of Maryland, College Park, Maryland 20742, USA*
[2]*School of Space Research, Kyung Hee University, Yongin, Gyeonggi 17104, Korea*
[3]*Korea Astronomy and Space Science Institute, Daejeon 34055, Korea*
[4]*Space Sciences Laboratory, University of California, Berkeley, California 94720-7450, USA*
[5]*Lunar and Planetary Laboratory & Department of Planetary Science, University of Arizona,
Tucson, Arizona 85721-0092, USA*

Reliable models of the solar wind in the near-Earth space environment may constrain conditions close to the Sun. This is relevant to NASA's contemporary innerheliospheric mission *Parker Solar Probe*. Among the outstanding issues is how to explain the solar wind temperature isotropy. Perpendicular and parallel proton and electron temperatures near 1 AU are theoretically predicted to be unequal, but *in situ* observations show quasi-isotropy sufficiently below the instability threshold condition. This has not been satisfactorily explained. The present Letter shows that the dynamical coupling of electrons and protons via collisional processes and instabilities may contribute toward the resolution of this problem.

Characterizing physical processes that arise in the heliospheric environment helps to reveal the nature of similar processes occurring in other parts of the Universe. Accurately modeling the solar wind, from its acceleration at the Sun's surface through its evolution to 1 AU (astronomical unit) is essential for this characterization. Such models will be tested against *in situ* observations from the contemporary *Parker Solar Probe* [1], which will provide *in situ* data from the unprecedented close vicinity of the Sun.

Among the outstanding issues associated with the solar wind near 1 AU is the solar wind isotropy problem. According to standard models, the radially expanding solar wind is supposed to develop temperature anisotropy as a result of the conservation of adiabatic moments. However, solar wind measured in the near-Earth region shows that protons and electrons are predominantly characterized by quasi-isotropic conditions that are sufficiently away from the instability threshold conditions, and only a small minority of cases exhibit mild anisotropy. In general, electrons are more isotropic than the protons [2–6].

Figures 1 and 2 display typical distributions of data near 1 AU. The proton data set comes from *Wind* spacecraft Solar Wind Experiment Faraday cup observations [7] to which a nonlinear least squares fitting algorithm is applied to determine solar wind proton velocity moments, namely density, bulk speed, temperature, and temperature anisotropy [8]. The electron temperature anisotropy data set comes from a sophisticated analysis algorithm that analyzes solar wind electron velocity distribution functions measured by 3DP [9] correcting from spacecraft charging and other instrumental effects polluting the electrostatic

analyzer measurements [10,11]. The magnetic field was determined using the MFI magnetometers [12]. The resulting distributions are plotted in $(\beta_{\|a}, T_{\perp a}/T_{\|a})$ parameter space, where $\beta_{\|a} = 8\pi n_a T_{\|a}/B^2$ ($a = p$, e for protons and
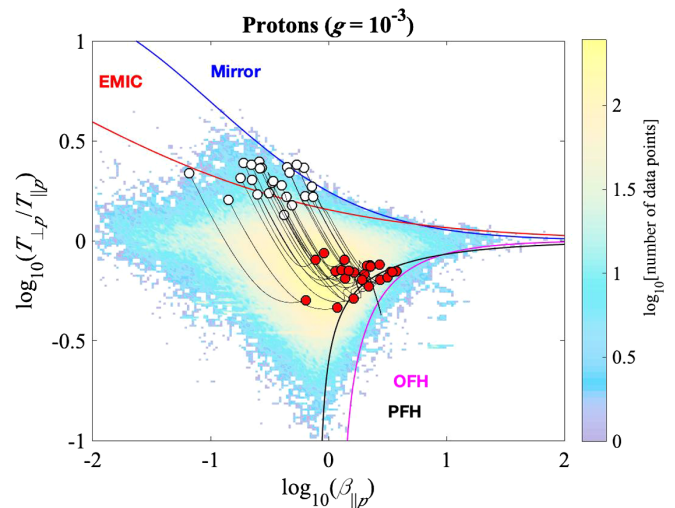

FIG. 1. Proton data distribution, which shows that the marginal mirror instability condition defines the upper-right boundary, although the electromagnetic ion-cyclotron (EMIC) threshold condition could also partially contribute. For the lower-right boundary, proton (PFH for parallel and OFH for oblique) firehose instability threshold conditions can be associated with. Superposed is the progression of proton beta and temperature anisotropy from initial (open circles) to final state (red circles) computed theoretically. The proton data set comes from *Wind* spacecraft Solar Wind Experiment Faraday cup observations.
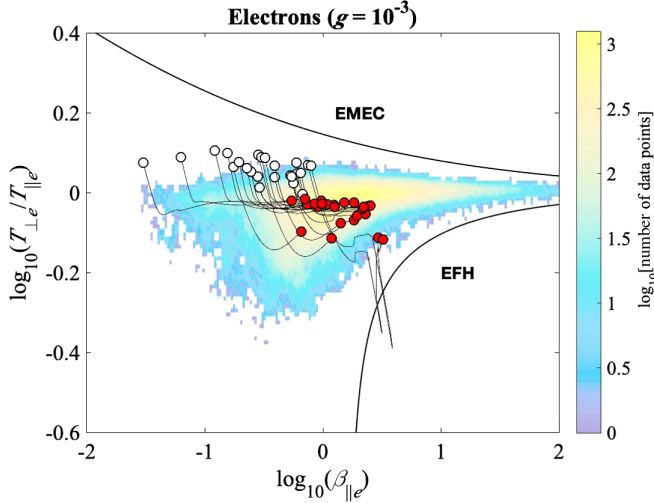
FIG. 2. Electron data distribution, which shows that the upper-right boundary is defined by the electromagnetic electron-cyclotron (EMEC) instability threshold, while the electron firehose (EFH) instability curve defines the lower-right boundary. While they circumscribe the distribution for large $\beta_{\parallel e}$, data points are located significantly far away from the marginal instability curves. Superposed is the progression of the electron beta and temperature anisotropy from initial (open circles) to final state (red circles) computed theoretically. The electron data set comes from the *Wind* spacecraft 3DP instrument. The magnetic field was determined using the magnetic field investigation (MFI) magnetometers.

electrons) represents the plasma beta defined via parallel temperature $T_{\parallel a}$ for each species, n_a and B being the ambient density and magnetic field intensity, respectively, and $T_{\perp a}$ denotes the perpendicular temperature [2–6]. Various temperature anisotropy-driven instabilities partially define the outer boundaries for departures from isotropy. The empirical marginal stability curves, represented by $T_{\perp p}/T_{\parallel p} = 1 + S(\beta_{\parallel a} - \beta_{\parallel 0})^{-a}$, where S, $\beta_{\parallel 0}$, and a are empirical fitting parameters constructed by solving linear dispersion relations for various instabilities with bi-Maxwellian velocity distribution functions for protons and electrons. The values for these parameters can be found in Refs. [13–15]. The apparent boundaries to the left-hand side remain largely unexplained, but it could be the combined result of propagation along the spiraling solar wind magnetic field [16] and Alfvén-cyclotron resonant heating [17,18]. A feature that cannot be explained by instabilities alone is that most data points are located far from the stability thresholds, and are broadly accumulated near isotropic states. To our knowledge, few models satisfactorily account for this feature.

Currently available self-consistent models—expanding box hybrid simulations [19–24] and kinetic-fluid models [25–27]—predict that the proton data distribution near 1 AU should accumulate near the firehose (FH) instability threshold curve—see, e.g., [22,26]. This is because in both

the customary quasilinear theory for low-frequency instabilities [28,29] and hybrid simulations [19–24] the electrons are treated as a background fluid, and thus are dynamically unimportant. Recently, however, fully kinetic simulation of expanding box solar wind is being carried out, which may partially confirm the theory to be presented subsequently [30]. Note, however, that this work does not have explicit collisional dissipation in the simulation scheme, but finite electron mass may allow dynamical coupling of protons and electrons via collective effects.

Collisions in the solar wind are infrequent, but the cumulative "collisional age" effect is known to contribute toward the isotropization of the proton temperatures [17,31]. Other mechanisms proposed to resolve the isotropy problem include the large scale variations of background density and magnetic field [27,32], or intermediate-scale *saptiotemporal* variations due to compressive fluctuations [33]. The perpendicular heating of protons by Alfvén-cyclotron resonance [17,18] or by turbulence [34] may also contribute to the isotropization.

Reference [35], on the other hand, demonstrated the proton isotropization (but not the electrons) by considering dynamical coupling between the protons and electrons via electron firehose (EFH) instability. This work can be contrasted to those of Refs. [27,31], where collisional relaxation is included but not the dynamically coupled electrons and protons through instability. On the other hand, while Ref. [35] does include dynamically coupled electrons and protons, it does not include collisional relaxation effects. The isotropization of both species requires binary collisions in addition to the instabilities. This is in agreement with Salem *et al.* [36], who analyzed the *Wind* spacecraft data and concluded that the Coulomb collisions are important for the electrons. A similar conclusion for ions was also reached by Kasper *et al.* [37] and Kasper *et al.* [38], who showed that some measures of departure from thermodynamic equilibrium are best organized by collisional age. Binary collisions are customarily treated on the basis of unmagnetized plasma theory. For solar wind near 0.3 AU, or even closer, near ∼10 solar radii (where the *Parker Solar Probe* will eventually survey), it is more appropriate to employ the magnetized plasma theory [39].

The present steady-state model based upon the assumption of bi-Maxwellian velocity distributions (which was tested against particle-in-cell simulation, see, e.g., Refs. [40,41]) describes the evolution of perpendicular and parallel temperatures for protons and electrons subject to radial expansion (exp), plasma instabilities (inst) propagating in parallel direction, and collisional age (coll) effects:

$$\frac{d\beta_{\perp p,e}}{dX} = \left(\frac{d}{dX}\bigg|_{\text{coll}} + \frac{d}{dX}\bigg|_{\text{inst}} \right)\beta_{\perp p,e},$$

$$\frac{d\beta_{\parallel p,e}}{dX} = \left(\frac{d}{dX}\bigg|_{\text{exp}} + \frac{d}{dX}\bigg|_{\text{coll}} + \frac{d}{dX}\bigg|_{\text{inst}} \right)\beta_{\parallel p,e}, \quad (1)$$

where normalized temperatures (betas) are defined by $\beta_{\perp,\parallel a} = 8\pi n(r_0) T_{\perp,\parallel a}/[fB^2(r_0)]$, $a = p, e$. In Eq. (1), $X = \Omega_i(r_0)r/V$ is the normalized radial distance, r_0 (or dimensionless X_0) being the "sunward" boundary, V represents (constant) solar wind speed, and $\Omega_p(r_0) = eB(r_0)/m_p c$ stands for proton gyrofrequency at r_0. The quantity $f(r) = B(r)/B(r_0) = n(r)/n(r_0)$, is the inhomogeneity scale form factor for solar wind density and magnetic field intensity. The collisional age effect is described by

$$(d\beta_{\perp p}/dX)_{\text{coll}} = \nu_{pp}(\beta_{\parallel p} - \beta_{\perp p}),$$
$$(d\beta_{\parallel p}/dX)_{\text{coll}} = \nu_{pe}(\beta_{\parallel e} - \beta_{\parallel p}) - 2\nu_{pp}(\beta_{\parallel p} - \beta_{\perp p}),$$
$$(d\beta_{\perp e}/dX)_{\text{coll}} = \nu_{ee}(\beta_{\parallel e} - \beta_{\perp e}),$$
$$(d\beta_{\parallel e}/dX)_{\text{coll}} = \nu_{pe}(\beta_{\parallel p} - \beta_{\parallel e}) - 2\nu_{ee}(\beta_{\parallel e} - \beta_{\perp e}), \quad (2)$$

where normalized collisional relaxation frequencies, derived under the assumption of bi-Maxwellian particle distributions, are given by [39]

$$\nu_{pp} = \frac{c_1 g \beta_{\perp p}^{3/2}(X_0) f(X)}{\beta_{\perp p}(X)\beta_{\parallel p}^{1/2}(X)},$$

$$\nu_{pe} = \frac{\mu^{1/2} c_0 g \beta_{\perp p}^{3/2}(X_0) f(X)}{2^{3/2}[\mu\beta_{\parallel p}(X) + \beta_{\parallel e}(X)]^{3/2}},$$

$$\nu_{ee} = \frac{c_1 g \beta_{\perp p}^{3/2}(X_0) f(X)}{\mu^{1/2}\beta_{\perp e}(X)\beta_{\parallel e}^{1/2}(X)}, \quad (3)$$

and $\mu = m_e/m_p$ represents the electron-to-proton mass ratio. The parameter g is defines the collisionality of magnetized plasma, $g = [n_0(r_0)\rho_p^3(r_0)]^{-1}(c/v_{A0})^4$, where $\rho_p(r_0) = [2T_{\parallel p}(r_0)/m_p\Omega_p^2(r_0)]^{1/2}$ designates the proton thermal gyro radius defined at r_0, and $v_{A0} = B(r_0)/\sqrt{4\pi n(r_0)m_p}$ is the reference Alfvén speed. Typical values for g in the solar wind near 1 AU is of the order $g \sim \mathcal{O}(10^{-6})$, but in the vicinity of the coronal source region, it can be substantially higher [31]. The coefficients $c_0 \sim 0.21$ and $c_1 \sim 0.03$ are defined in Ref. [27].

The radial expansion, which only affects parallel betas, is described by

$$(d\beta_{\parallel p,e}/dX)_{\text{exp}} = f^{-1}(df/dX)\beta_{\parallel p,e}. \quad (4)$$

The radial expansion factor f adopted in the present study is given by a simple Lorentzian form, $f(r) = [1 + (r/R_*)^2]^{-1} = [1 + (X/X_*)^2]^{-1}$. Here, R_* or its normalized form X_* is the scale height of the radial inhomogeneity. The contribution from instabilities is specified by

$$\left.\frac{d\beta_{\perp p}}{dX}\right|_{\text{inst}} = f\sum_{+,-}\int\frac{d\kappa}{\kappa^2}\mathcal{W}_{\mp}(\kappa)\{(2A_p + 1)z_i$$
$$+\text{Im}[(2iz_i \mp 1)\eta_p Z(\zeta_p)]\},$$

$$\left.\frac{d\beta_{\parallel p}}{dX}\right|_{\text{inst}} = 2f\sum_{+,-}\int\frac{d\kappa}{\kappa^2}\mathcal{W}_{\mp}(\kappa)\{(A_p + 1)z_i$$
$$+\text{Im}[(z \mp 1)\eta_p Z(\zeta_p)]\},$$

$$\left.\frac{d\beta_{\perp e}}{dX}\right|_{\text{inst}} = f\sum_{+,-}\int\frac{d\kappa}{\kappa^2}\mathcal{W}_{\mp}(\kappa)\left\{\frac{(2A_e + 1)z_i}{\mu}\right.$$
$$\left.+\text{Im}\left[\left(2iz_i \pm \frac{1}{\mu}\right)\eta_e Z(\zeta_e)\right]\right\},$$

$$\left.\frac{d\beta_{\parallel e}}{dX}\right|_{\text{inst}} = 2f\sum_{+,-}\int\frac{d\kappa}{\kappa^2}\mathcal{W}_{\mp}(\kappa)\left\{\frac{(A_e + 1)z_i}{\mu}\right.$$
$$\left.+\text{Im}\left[\left(z \pm \frac{1}{\mu}\right)\eta_e Z(\zeta_e)\right]\right\}, \quad (5)$$

where $\mathcal{W}_{\mp}(\kappa) = \delta B^2(k)/[f^2 B_0^2(r_0)]$ is the dimensionless spectral wave magnetic field energy density, which is solved from the wave kinetic equation, $\partial\mathcal{W}(\kappa)/\partial X = 2f^{1/2}z_i\mathcal{W}(\kappa)/v_g$. Here, $v_g = \partial z/\partial\kappa$ is the wave group speed. Various quantities in Eq. (5), are defined by $A_a = \beta_{\perp a}/\beta_{\parallel a} - 1$, for $a = e, p$; $z = \omega/\Omega_p(r)$ and $\kappa = ck/\omega_{pp}(r)$, z_i being the imaginary part of z; $\eta_p = [(A_p + 1)z \mp A_p]/(\kappa\theta_{\parallel p}^{1/2})$; $\eta_e = [(A_e + 1)z \mp A_e/\mu]/(\kappa\theta_{\parallel e}^{1/2})$; $\zeta_p = (z \pm 1)/(\kappa\theta_{\parallel p}^{1/2})$; and $\zeta_e = (z \pm 1/\mu)/[\kappa(\theta_{\parallel e}/\mu)^{1/2}]$. Here, $\omega_{pp} = [4\pi n(r)e^2/m_p]^{1/2}$ is the proton plasma frequency. The plasma dispersion function $Z(\zeta) = \pi^{-1/2}\int_{-\infty}^{\infty} dx e^{-x^2}(x - \zeta)^{-1}$ is well known. The complex frequency z is determined from the local dispersion relation,

$$0 = \kappa^2 - A_p - A_e/\mu - \eta_p Z(\zeta_p) - \eta_e Z(\zeta_e). \quad (6)$$

We have taken into account both left- and right-hand circularly polarized modes propagating in parallel direction. We employed the leapfrog scheme, coupled with complex root solver.

Figures 1 and 2 superpose theoretical results on top of data distributions. We considered a small collection of proton and electron ensembles at the sunward boundary $X = 0$ (representing 0.3 AU). The initial ensemble points are plotted with open circles. The protons are taken to be slightly above or close to the proton-cyclotron instability threshold near $X = 0$, which is typical of solar wind conditions observed by the *HELIOS* spacecraft [42]. The electrons at $X = 0$ are assumed to be stable, which is typical of the solar wind near 0.3 AU [3]. The final states (representing 1 AU) are indicated by red dots, with intermediate paths connecting the initial and final states. We considered a scaled system size, which is substantially
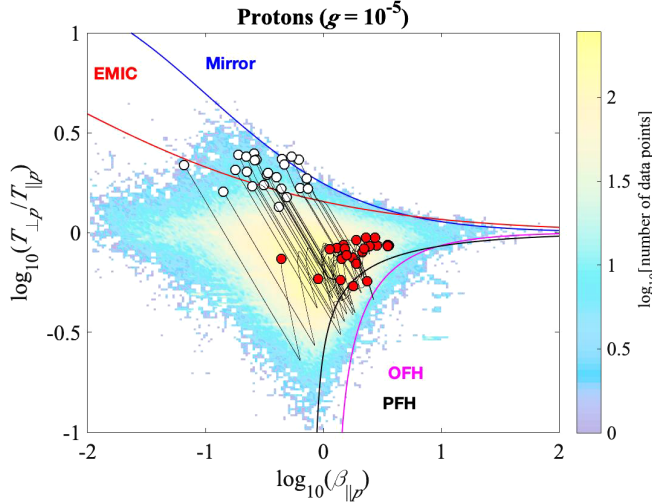
FIG. 3. The same as Fig. 1, except that a lower value of g parameter corresponding to 10^{-5} is adopted. Nonlinear progression of proton beta and temperature anisotropy from initial (open circles) to final state (red circles) shows that the proton isotropization is achieved.
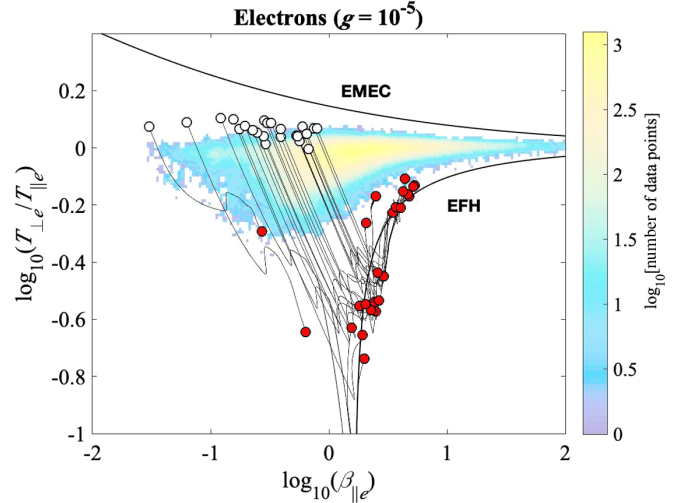
FIG. 4. Nonlinear progression of electron beta and temperature anisotropy from initial (open circles) to final state (red circles). Final states are all close to the EFH marginal stability.

smaller compared with actual solar wind scales. Specifically, we chose $X_{\max} = \Omega_i r_{\max}/V_{sw} = 4 \times 10^4$, with the scale height of $X_* = 10^4$. This was done to facilitate numerical computation. We also adopted the value $g = 10^{-3}$ for the collisional parameter. This choice is supposed to represent a situation where collisions are significant.

Figure 1 shows that the final states are quasi-isotropic for both protons and electrons, all being located away from the marginal stability curves, which shows that electron isotropization requires the inclusion of collisional relaxation in addition to dynamically coupled protons and electrons via instability.

To further confirm this, we chose a lower value of $g = 10^{-5}$. With such a choice, we find that, while the proton isotropization is achieved via instability, the final states for electrons are all close to the EFH marginal stability curve, in agreement with Ref. [35] (for which $g = 0$)—see Figs. 3 and 4.

Before we close, we discuss a number of caveats. One of them relates to the interrelationship between the inverse scale height R_* and the g parameter, $\mathcal{O}[(R^*)^{-1}] : \mathcal{O}(g)$. In our model we chose the dimensionless scale height of $X_* = 10^4$. For 0.3 AU $= 4.486 \times 10^7$ km, the average proton-cyclotron frequency is $f_{cp} = 1.4226$ Hz, or $\Omega_p = 8.9385$ Hz/rad. For a solar wind speed of ~ 100 km/s, the choice of $X_{\max} = 4 \times 10^4$ translates to $r_{\max} = X_{\max} V_{sw}/\Omega_i \sim 10^6$ km, which is at least 2 orders of magnitude lower than the actual net distance between 0.3 and 1 AU, or $\sim 10^8$ km. This implies that the effective R_* should be at least 2 orders of magnitude higher than our choice. Since the effects of g is inversely proportional to R_*, the realistic critical g parameter is expected to be at least 2 orders lower than

$g = 10^{-3}$. We have in fact, ran a sample case with 2 orders of magnitude higher X_* and similar 2 orders of magnitude lower g and found qualitatively similar result. The precise value of realistic g parameter depends on a number of solar wind variables, but observations generally show that collisional effects seem to be more pronounced for slow solar wind than fast wind conditions [43]. Observational determination of the g parameter remains an outstanding task.

In our model, we adopted a simple Lorentzian density/B field scale function f. However, in order to accurately reflect the actual solar wind evolution from solar source to 1 AU and beyond, one could improve the form factor f. Based primarily on averaged extrapolations from *HELIOS* data, it is possible to deduce separate scaling functions for n and B, namely, $f_n(r) = n(r)/n_0 = (r/R_\odot)^{-1.02}$ and $f_B(r) = B(r)/B_0 = (r/R_\odot)^{-2} + 10^{-2}(r/R_\odot)^{-1.4} + 3 \times 10^{-4}(r/R_\odot)^{-0.8}$, where $R_\odot$ is the solar radius. In the future, we plan to extend the present model calculation by incorporating the above more realistic form factors.

It is possible to include the effect of spiraling magnetic field, following the approach in Refs. [44] and [45], for instance. Hellinger [46] employed the expanding box hybrid simulation and demonstrated that the solar wind expansion path along the spiraling B field is not a straight diagonal line in $(\beta_{\parallel p}, T_{\perp p}/T_{\parallel p})$ space, but is deflected depending on the spiral angle.

It is well known that solar wind electrons consist of denser core population and hotter tenuous halo component. The fast wind also features a field-aligned *strahl* component. The protons are also sometimes observed to be composed of core and beam components. Alpha particles are also measured to stream away from the Sun, with a net alpha-proton relative drift speed. In principle, our model could be generalized to include the core and halo or beam

dual component structure. The core-halo electrons involve the heat flux relaxation and instability excitation [47,48].

Obliquely propagating instabilities could, in principle, be included in the present scheme. The effects of such instabilities are relevant to refined marginal stability conditions. While all of the above aspects belong to future research, it is important to note that the major finding of the present Letter is composed of identifying the mechanism of combined instabilities and binary collisions opposing radial expansion effects, which may contribute to a potential resolution of the solar wind temperature isotropy problem.

The data used in this project were accessed through SPFD CDA following the link in Ref. [49].

---

*yoonp@umd.edu

[1] N. J. Fox, M. C. Velli, S. D. Bale, R. Decker, A. Driesman, R. A. Howard, J. C. Kasper, J. Kinnison, M. Kusterer, D. Lario *et al.*, Space Sci. Rev. **204,** 7 (2016).

[2] J. C. Kasper, A. J. Lazarus, S. P. Gary, and A. Szabo, AIP Conf. Proc., **679,** 538 (2003).

[3] Š. Štverák, P. Trávníček, M. Maksimovic, E. Marsch, A. N. Fazakerley, and E. E. Scime, J. Geophys. Res. **113,** A03103 (2008).

[4] S. D. Bale, J. C. Kasper, G. G. Howes, E. Quataert, C. Salem, and D. Sundkvist, Phys. Rev. Lett. **103,** 211101 (2009).

[5] P. Hellinger and P. Trávníček, Astrophys. J. Lett. **784,** L15 (2014).

[6] C. H. K. Chen, L. Matteini, A. A. Schekochihin, M. L. Stevens, C. S. Salem, B. A. Maruca, M. W. Kunz, and S. D. Bale, Astrophys. J. Lett. **825,** L26 (2016).

[7] K. W. Ogilvie, D. J. Chornay, R. J. Fritzenreiter, F. Hunsaker, J. Keller, J. Lobell, G. Miller, J. D. Scudder, J. Sittler, E. C., R. B. Torbert *et al.*, Space Sci. Rev. **71,** 55 (1995).

[8] B. A. Maruca and J. C. Kasper, Adv. Space Res. **52,** 723 (2013).

[9] R. P. Lin, K. A. Anderson, S. Ashford, C. Carlson, D. Curtis, R. Ergun, D. Larson, J. McFadden, M. McCarthy, G. K. Parks *et al.*, Space Sci. Rev. **71,** 125 (1995).

[10] C. S. Salem, M. Pulupa, S. D. Bale, and D. Verscharen, Astrophys. J. Suppl. (to be published).

[11] M. Pulupa, S. D. Bale, C. Salem, and K. Horaites, J. Geophys. Res. **119,** 647 (2014).

[12] R. P. Lepping, M. H. Acũna, L. F. Burlaga, W. M. Farrell, J. A. Slavin, K. H. Schatten, F. Mariani, N. F. Ness, F. M. Neubauer, Y. C. Whang *et al.*, Space Sci. Rev. **71,** 207 (1995).

[13] S. P. Gary and J. Wang, J. Geophys. Res. **101,** 10749 (1996).

[14] S. P. Gary, J. Wang, D. Winske, and S. A. Fuselier, J. Geophys. Res. **102,** 27159 (1997).

[15] P. Hellinger, P. Trávníček, J. C. Kasper, and A. J. Lazarus, Geophys. Res. Lett. **33,** L09101 (2006).

[16] L. Matteini, P. Hellinger, S. Landi, P. Trávníček, and M. Velli, Space Sci. Rev. **172,** 373 (2012).

[17] S. R. Cranmer, Astrophys. J. Suppl. Ser. **213,** 16 (2014).

[18] N. Ozak, L. Ofman, and A.-F. Viñas, Astrophys. J. **799,** 77 (2015).

[19] P. C. Liewer, M. Velli, and B. E. Goldstein, J. Geophys. Res. **106,** 29261 (2001).

[20] P. Hellinger, P. Trávníček, A. Mangeney, and R. Grappin, Geophys. Res. Lett. **30,** 1211 (2003).

[21] L. Matteini, S. Landi, P. Hellinger, and M. Velli, J. Geophys. Res. **111,** A10101 (2006).

[22] P. Hellinger and P. Trávníček, J. Geophys. Res. **113,** A10109 (2008).

[23] P. Hellinger and P. Trávníček, J. Geophys. Res. **118,** 5421 (2013).

[24] L. Ofman, A. F. Viñas, and Y. Maneva, J. Geophys. Res. **119,** 4223 (2014).

[25] B. D. G. Chandran, T. J. Dennis, E. Quataert, and S. D. Bale, Astrophys. J. **743,** 197 (2011).

[26] P. H. Yoon and J. Seough, J. Geophys. Res. **119,** 7108 (2014).

[27] P. H. Yoon, Astrophys. J. **833,** 106 (2016).

[28] J. Seough and P. H. Yoon, J. Geophys. Res. **117,** A08101 (2012).

[29] P. H. Yoon and J. Seough, J. Geophys. Res. **117,** A08102 (2012).

[30] M. E. Innocenti, A. Tenerani, and M. Velli, Astrophys. J. **870,** 66 (2019).

[31] P. H. Yoon, J. Geophys. Res. **121,** 10,665 (2016).

[32] J. Seough, P. H. Yoon, K.-H. Kim, and D.-H. Lee, Phys. Rev. Lett. **110,** 071103 (2013).

[33] D. Verscharen, B. D. G. Chandran, K. G. Klein, and E. Quataert, Astrophys. J. **831,** 128 (2016).

[34] S. Servidio, K. T. Osman, F. Valentini, D. Perrone, F. Califano, S. Chapman, W. H. Matthaeus, and P. Veltri, Astrophys. J. **781,** L27 (2014).

[35] P. H. Yoon and M. Sarfraz, Astrophys. J. **835,** 246 (2017).

[36] C. Salem, D. Hubert, C. Lacombe, S. D. Bale, A. Mangeney, D. E. Larson, and R. P. Lin, Astrophys. J. **585,** 1147 (2003).

[37] J. C. Kasper, A. J. Lazarus, and S. P. Gary, Phys. Rev. Lett. **101,** 261103 (2008).

[38] J. C. Kasper, K. G. Klein, T. Weber, M. Maksimovic, A. Zaslavsky, S. D. Bale, B. A. Maruca, M. L. Stevens, and A. W. Case, Astrophys. J. **849,** 126 (2017).

[39] P. H. Yoon, Phys. Plasmas **23,** 072114 (2016).

[40] J. Seough, P. H. Yoon, and J. Hwang, Phys. Plasmas **21,** 062118 (2014).

[41] J. Seough, P. H. Yoon, and J. Hwang, Phys. Plasmas **22,** 012303 (2015).

[42] L. Matteini, S. Landi, P. Hellinger, F. Pantellini, M. Maksimovic, M. Velli, B. E. Goldstein, and E. Marsch, Geophys. Res. Lett. **34**, L20105 (2007).

[43] J. C. Kasper, K. G. Klein, T. Weber, M. Makimovic, A. Zaslavsky, S. D. Bale, and B. A. Maruca, Astrophys. J. **849**, 126 (2017).

[44] J. L. Phillips, J. T. Gosling, D. J. McComas, S. J. Bame, and S. P. Gary, J. Geophys. Res. **94**, 6563 (1989).

[45] P. J. L. and J. T. Gosling, J. Geophys. Res. **95**, 4217 (1990).

[46] P. Hellinger, J. Plasma Phys. **83**, 705830105 (2017).

[47] S. Saeed, M. Sarfraz, P. H. Yoon, M. Lazar, and M. N. S. Qureshi, Mon. Not. R. Astron. Soc. **465**, 1672 (2017).

[48] S. M. Shaaban, M. Lazar, P. H. Yoon, and S. Poedts, Phys. Plasmas **25**, 082105 (2018).

[49] See https://cdaweb.gsfc.nasa.gov.